Earth and Planetary Science Letters 614 (2023) 118195

Contents lists available at ScienceDirect

Earth and Planetary Science Letters

journal homepage: www.elsevier.com/locate/epsl

Inconsistent mercury records from terrestrial upland to coastal lowland across the Permian-Triassic transition

Jianbo Chen [a,b,1], Guangyi Sun [c,1], Binjian Lu [a,c], Rong-yao Ma [a], Zhuang Xiao [d], Yao-feng Cai [b], Hua Zhang [b], Shu-zhong Shen [e], Feifei Zhang [e,*], Zhuo Feng [a,*]

[a] Institute of Palaeontology, Yunnan Key Laboratory of Earth System Science, Yunnan Key Laboratory for Palaeobiology, Yunnan University, Kunming 650500, China
[b] State Key Laboratory of Palaeobiology and Stratigraphy, Nanjing Institute of Geology and Palaeontology, Chinese Academy of Sciences, Nanjing 210008, China
[c] State Key Laboratory of Environmental Geochemistry, Institute of Geochemistry, Chinese Academy of Sciences, Guiyang 550081, China
[d] School of Earth Sciences, Yunnan University, Kunming 650500, China
[e] State Key Laboratory for Mineral Deposits Research, School of Earth Sciences and Engineering, and Frontiers Science Center for Critical Earth Material Cycling, Nanjing University, Nanjing 210023, China

ARTICLE INFO

Article history:
Received 1 December 2022
Received in revised form 25 April 2023
Accepted 27 April 2023
Available online 12 May 2023
Editor: A. Jacobson

Keywords:
mercury enrichments
mercury isotopes
terrestrial sediments
Permian–Triassic extinction
volcanism

ABSTRACT

The enrichment of mercury (Hg) in sediments has been increasingly utilized as a proxy for large-scale volcanism. However, a causal link between these two remains ambiguous, as Hg enrichments can be caused by many non-volcanic factors, e.g., changes in local depositional environments or terrestrial runoffs. In this study, we present high-resolution Hg concentration and isotope records of two drill cores, one located in a coastal lowland (HK-1) and the other in a terrestrial upland (TK-1), spanning the Permian–Triassic boundary (PTB). Interestingly, the coastal lowland core exhibits significant Hg enrichments over a stratigraphic horizon of approximately 200 meters (corresponding to a duration of ~2 Myrs), with dominating negative Δ^{199}Hg values. In contrast, the terrestrial upland core primarily displays background Hg levels with near-zero Δ^{199}Hg values. Given the spatial proximity of the two cores, separated by only about 70 km, we interpret these discrepant Hg signatures to indicate that terrestrial upland underwent minimal influence from terrestrial and/or atmospheric depositions rather than volcanic input, while the coastal lowland was primarily sourced from enhanced terrestrial influxes, depositing under oxygen-deficient conditions. This interpretation is supported by the high concentrations of organic carbon and sulfur, substantial pyrite layers, and positive correlations between Hg and chalcophile elements, such as Mo, Se, and Co, in the HK-1 core. Our study highlights the need to examine multiple Hg enrichment factors in sedimentary records before comprehensively establishing a robust causal link with volcanic activities. A thorough evaluation of multiple lines of evidence, including Hg isotopes, local environmental proxies, and sedimentology investigations, should be conducted first, particularly necessary for the non-marine sediments.

1. Introduction

The end-Permian mass extinction (EPME, ~252 million years ago) was the most severe biotic crisis in the history of life on Earth, with estimated losses of >81% of marine and >89% of terrestrial species within approximately 60 ka (Sepkoski, 1984; Fan et al., 2020). The large-scale volcanism, including the Siberian Traps large igneous province (STLIP) and arc magmatism from around the Paleo-, Meso- and Neo-Tethys oceans, have been invoked as the ultimate trigger for a series of environmental perturbations leading to the catastrophic event (Burgess et al., 2017; Chen and Xu, 2019; Zhang et al., 2021). As mercury from volcanic degassing can be transported rapidly through global atmospheric circulation (Pyle and Mather, 2003; Lyman et al., 2020), Hg enrichments in marine sediments around the Permian–Triassic boundary (PTB) have been widely regarded as direct evidence supporting a causal link between volcanism and the EPME (Fig. 1). Recent reports on terrestrial sedimentary Hg records also highlighted the role of volcanism in driving terrestrial ecosystem disturbance (Shen et al., 2019a; Chu et al., 2020, 2021; Wang et al., 2021). However, sedimentary Hg enrichments can be affected by several non-volcanic factors, such as intensified terrestrial runoffs and/or changes in lo-

* Corresponding authors.
E-mail addresses: fzhang@nju.edu.cn (F. Zhang), zhuofeng@ynu.edu.cn (Z. Feng).
[1] The authors contribute equally.

https://doi.org/10.1016/j.epsl.2023.118195
0012-821X/

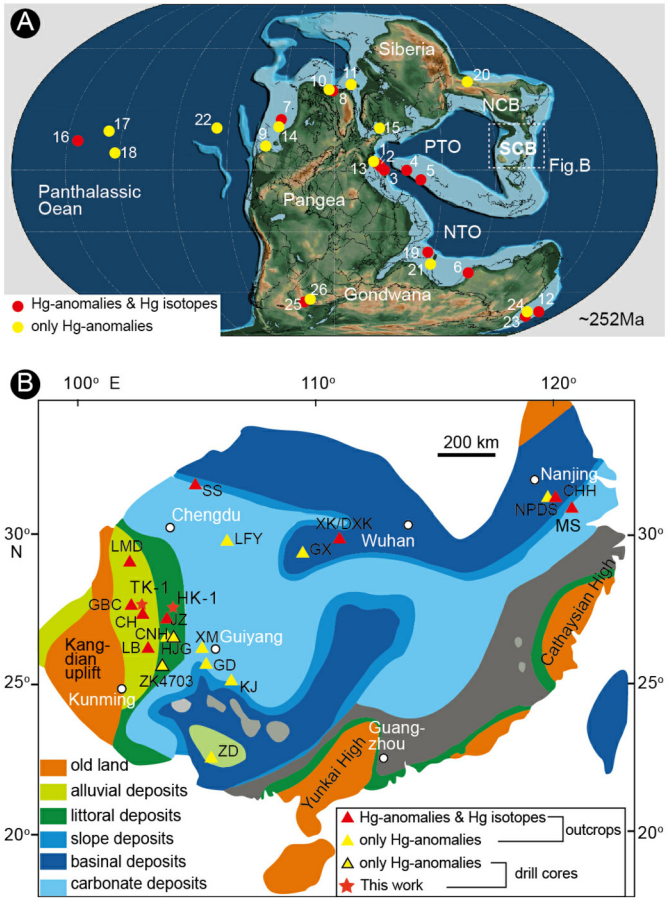

Fig. 1. Mercury studies within the Permian–Triassic transitional period (~252 Ma) on global paleogeography (A) and South China Block (B). Site numbers in A and acronyms for sections in B are given in Supplementary Data S1. NCB—North China Block; SCB—South China Block; PTO—Paleo-Tethys Ocean; NTO—Neo-Tethys Ocean.

cal depositional environments (Bergquist, 2017; Zheng et al., 2018; Them et al., 2019; Shen et al., 2022), leaving a precise causal link between volcanism and the EPME ambiguous. This is particularly the case for interpreting mercury anomalies in the terrestrial and nearshore sediments, as the contribution by terrestrial runoffs into non-marine sediments remains poorly evaluated. In addition, it is worth noting that, except for a few studies based on fresh drill core samples (Fig. 1B; Chu et al., 2020; Shen et al., 2022), most Hg signatures were obtained from outcrop samples, which might have suffered from alterations due to the effect of intensive surface weathering and post-depositional degradation of organic matter (Charbonnier et al., 2020; Chen et al., 2022; Park et al., 2022).

Mercury isotopes provide powerful tools for tracing sources and pathways of sedimentary Hg anomaly (Blum et al., 2014; Bergquist, 2017). Although the mass-dependent fractionation (MDF, often represented by δ^{202}Hg) of Hg isotopes can be caused by various physical, chemical, and biological processes during the Hg cycle, their mass-independent fractionations (MIF) are primarily generated during photochemical processes (Blum et al., 2014; Blum and Johnson, 2017). The odd-Hg MIF (represented by Δ^{199}Hg and Δ^{201}Hg) is now used as a primary tracer to distinguish volcanic Hg sources, where sedimentary Hg enrichment without measurable Δ^{199}Hg values (~0‰) reflects source by volcanism (Zambardi et al., 2009; Sun et al., 2016; Si et al., 2020). In contrast, sedimentary Hg enrichment with positive Δ^{199}Hg values likely indicates direct atmospheric Hg deposition, and negative Δ^{199}Hg reflects either enhanced terrestrial input (Shen et al., 2019b) or shallow water euxinia (Zheng et al., 2018).

In this paper, we provide high-resolution Hg concentration and isotope records of drill cores in Southwest China, which is the first detailed comparative study on Hg anomalies, Hg isotopes, and their mineral hosts from two distinct non-marine PTB settings. The two cores provide a unique opportunity to examine how terrestrial sedimentary Hg is affected by factors such as volcanic, terrestrial, and local depositional environments. We also explore the geochemical behavior of Hg in terms of land-marine teleconnection and likely shed light on a potentially diachronic terrestrial ecosystem collapse during the EPME.

2. Materials and methods

2.1. Geological setting and studied drill cores

The upper Permian to Lower Triassic outcrops widely in Southwest China, where marine and non-marine PTB sections have been extensively studied (Shen et al., 2011; Zhang et al., 2016; Chu et al., 2020; Feng et al., 2020a; Zhang et al., 2021; Chen et al., 2022). Non-marine upper Permian to Triassic sequences in this region, overlying unconformably the Emeishan Basalt, consists of the upper Permian Xuanwei Formation (Fm.), the Permian–Triassic transitional Kayitou Fm., and the Lower Triassic Dongchuan Fm. (terrestrial deposits) or Feixianguan Fm. (coastal deposits) in ascending order.

The Xuanwei Fm. mainly consists of alluvial deposits containing a highly diversified Cathaysian *Gigantopteris* flora and several coal beds. The uppermost coal seam in this formation is overlain diachronous by the Kayitou Fm., exhibiting similar lithological characteristics. The Kayitou Fm. is diachronous in southwestern China, most of which belongs to the uppermost Permian but partly to the Lower Triassic, based on the ID-TIMS U-Pb dating and the negative shift of organic carbon isotopes (Shen et al., 2011; Zhang et al., 2016; Chu et al., 2020). The Dongchuan Fm. overlying the uppermost yellow-greenish beds of the Kayitou Fm. composes maroon fine- to coarse-grained siliciclastic sediments. This formation has been interpreted as braided river deposits with rare plant fossils and abundant trough cross-bedding, parallel bedding, and scour structures (Zhang et al., 2016; Feng et al., 2020a). The Feixianguan Fm., composed of marine siliciclastic sandstones and mudstones with the typical Triassic fauna and floras, is thought to be synchronous with the Dongchuan Fm. of terrestrial settings (Zhang et al., 2016).

Two drill cores TK-1 (103°37′21″ E, 27°21′55″ N) and HK-1 (104°20′13″ E; 27°15′46″ N), were obtained from the terrestrial and coastal areas, respectively (Fig. S1). The TK-1 core was drilled in the Taoshujing section (E 103°37′21″ E, 27°21′55″ N) of the outskirt area in Zhaotong City, Yunnan Province. Typical terrestrial deposits with >40 individual palaeosols were recognized, although most are characterized by minimal pedogenic alteration with weak horizon development. The HK-1 core drill in the Lengqinggou section (104°20′13″ E; 27°15′46″ N) is located in Hezhang County, Guizhou Province. Its coastal deposits contain terrestrial–marine transitional facies during the Permian–Triassic transition (Cai et al., 2021).

2.2. Analytical procedures

Fine-grained core samples lacking visible veins were hand-picked and pulverized for analysis, including organic carbon isotope ($\delta^{13}C_{org}$), total organic carbon (TOC), total sulfur (TS), and elemental geochemistry.

For $\delta^{13}C_{org}$ and TOC analysis, samples were pre-treated with dilute hydrochloric acid to remove any carbonates. For TOC analysis, rinsed and dried samples were combusted in an oxygen atmosphere at ~1100 °C, generating CO_2 from the conversion of carbon

measured by an infrared (IR) cell. The mass was converted to percent carbon using sample dry weight. For $\delta^{13}C_{org}$ analysis, samples were reacted offline with 100% H_3PO_4 for 24 hours at 25 °C, following which the carbon isotope composition of the generated CO_2 was measured on a Finnigan MAT 253 mass spectrometer. Delta values were calibrated by the international reference standard NBS-19 ($\delta^{13}C = +1.95‰$) and the Chinese national standard GBW04416 ($\delta^{13}C = +1.61 \pm 0.03‰$) and reported relative to Vienna Pee Dee Belemnite (V-PDB) with a precision of better than $\pm$ 0.1‰ based on duplicate analyses of GBW04416. The analysis was conducted at the State Key Laboratory of Organic Geochemistry, Guangzhou Institute of Geochemistry, Chinese Academy of Sciences.

Elemental geochemistry including major and trace elements was conducted at the ALS-Chemex Laboratory in Guangzhou, China. The contents of major elements were measured using X-ray fluorescence (XRF) and Inductively coupled plasma atomic emission spectroscopy (ICP-AES), with an analytical accuracy of <2% (XRF) and <10% (ICP). Trace elements were extracted from the dried powders using $HF/HNO_3/HClO_4$ digestions and then determined by inductively coupled plasma mass spectrometer (ICP-MS), with an analytical accuracy of <10%.

2.3. Hg concentration and isotopes

Total Hg concentrations were analyzed using a Direct Mercury Analyzer (DMA-80) at the Institute of Geochemistry, Chinese Academy of Sciences, Guiyang, China. About 200–400 mg of each sample was weighed out and analyzed. Results were calibrated to the National Standard Material GSR-4 (quartz sandstone with Hg concentration of 8±2 ng g^{-1}). One replicate sample and a standard were analyzed for every ten samples. Data quality was monitored via multiple analyses of GSR-4, yielding an analytical precision (2σ) of Hg concentration measurement is < 8%. The method recovery was determined to be 103.0 ± 7.6% (mean ± 2SD, n = 47, 94.3%–113.0%) for certified reference material GBW07405 (GSS-5, yellow-red soil, Hg concentration: 290 ± 30 ng g^{-1}).

The pyrolysis method was used to extract Hg (Biswas et al., 2008; Sun et al., 2013), and then isotopes were determined using a Nu-Plasma multi-collector inductively coupled plasma mass spectrometer at the Institute of Geochemistry, Chinese Academy of Sciences, Guiyang (Yin et al., 2016). The international standard NIST SRM 997 Tl was used for simultaneous instrumental mass bias correction of Hg, and 3% $SnCl_2$ solution was used to generate elemental Hg^0 before being introduced into the plasma. International standard NIST SRM 3133 was measured after every three unknowns to monitor the stability of the instrument. Hg-MDF compositions are reported in delta notation (δ) as per mil (‰) deviations from the NIST 3133, and δ^{202}Hg is most widely reported (Chen et al., 2012; Grasby et al., 2019):

$$\delta^{202}\mathrm{Hg} = \left[\left(\frac{^{202}\mathrm{Hg}}{^{198}\mathrm{Hg}} \right)_{\mathrm{sample}} \Big/ \left(\frac{^{202}\mathrm{Hg}}{^{198}\mathrm{Hg}} \right)_{\mathrm{NIST\,3133}} - 1 \right] \times 10^3.$$

Hg-MIF is reported with capital delta notation (Δ) and quantified as the deviation from the theoretically predicted by MDF laws (Blum et al., 2014):

$$\Delta^{xxx}\mathrm{Hg} = \delta^{xxx}\mathrm{Hg} - \beta \times \delta^{202}\mathrm{Hg},$$

where xxx = 199, 200, or 201, and β-values are 0.252, 0.502, and 0.752 for isotopes ^{199}Hg, ^{200}Hg, and ^{201}Hg, respectively, according to the kinetic MDF law.

The NIST 8610 standard solution (UM-Almadén) was measured every 10–15 samples as a secondary standard with results of δ^{202}Hg = −0.52 ± 0.10‰, Δ^{199}Hg = −0.03 ± 0.03‰, Δ^{200}Hg = 0.00 ± 0.03‰, and Δ^{201}Hg = −0.05 ± 0.04‰ ($\pm 2\sigma$, n = 30), consistent with previously reported values (Chen et al., 2012; Sun et al., 2013). A total of five replicated analyses of GSS-5 were also conducted, with results of δ^{202}Hg = −1.48 ± 0.08‰, Δ^{199}Hg = −0.31 ± 0.05‰, Δ^{200}Hg = 0.01 ± 0.07‰, and Δ^{201}Hg = −0.29 ± 0.06‰ ($\pm 2\sigma$, n = 5), in agreement with newest published data (Shi et al., 2023). Uncertainties reported in this study correspond to the larger value of either the measurement uncertainty of replicate digests of GSS-5 or the uncertainty of repeated measurements of NIST 8610.

2.4. Ternary isotope mixing model

The fraction of Hg derived from terrestrial sources (f_t) was calculated using a simplified three-component mixing model for all measured samples:

$$\Delta^{199}\mathrm{Hg}_{\mathrm{sample}} = f_t \times \Delta^{199}\mathrm{Hg}_t + f_v \times \Delta^{199}\mathrm{Hg}_v + (1 - f_t - f_v) \times \Delta^{199}\mathrm{Hg}_a. \quad (1)$$

Where $\Delta^{199}\mathrm{Hg}_{\mathrm{sample}}$ represents the measured Δ^{199}Hg value of the core sample. $\Delta^{199}\mathrm{Hg}_t$, $\Delta^{199}\mathrm{Hg}_v$, and $\Delta^{199}\mathrm{Hg}_a$ are compositions of three end-members (terrestrial, volcanogenic, and atmospheric, respectively). f_v is the fraction of volcanogenic Hg in the measurements.

$\Delta^{199}\mathrm{Hg}_t$ is the endmember of the dominant pathway through vegetation absorption, and its value is adopted from the most negative value in the PTB terrestrial sediments reported previously ($\Delta^{199}\mathrm{Hg}_t = -0.14‰$) (Zhang et al., 2021). $\Delta^{199}\mathrm{Hg}_v = 0‰$ represents modern volcanogenic Hg lacking odd-MIF (Zambardi et al., 2009; Sun et al., 2016; Si et al., 2020), and this endmember value is only valid for 'direct' volcanogenic input. Once the Hg has undergone atmospheric transport after being outgassed during volcanism, its Δ^{199}Hg values would be changed by photo-redox processes in the atmosphere and mixed with the background atmospheric Hg signals. Therefore, the f_v in the current model could only evaluate the presence of proximal volcanism whose Hg may be able to deposit in nearby regions, rather than the SLIP, which is thousands of kilometers away from the study region.

According to the latest review by Zhou et al. (2021), terrestrial deposition encompasses dry (62–74% of terrestrial deposition) and wet (26–38%) deposition, where dry deposition is separated into vegetation Hg uptake (gaseous elemental mercury (Hg(0)) and divalent mercury (Hg(II))), which accounts for 76% of terrestrial uptake, and deposition to non-vegetation surfaces (soils, snow, and water; 24% of uptake). Therefore, there is approximately 47–56% of Hg uptaken by vegetation, ~15–18% of Hg deposition through non-vegetation dry deposition, and 26–38% through non-vegetation wet deposition. Since the terrestrial material mostly represents the atmospheric Hg(0) deposition, it is more appropriate to assume an atmospheric wet deposition end-member rather than the bulk atmosphere to avoid a double count. Therefore, $\Delta^{199}\mathrm{Hg}_a$ is the atmospheric wet deposition endmember (Chen et al., 2012; Zheng et al., 2020), and its value is adopted from the median value of Hg(II) rainfall which was summarized by a recent study ($\Delta^{199}\mathrm{Hg}_a = +0.40‰$ from Jiskra et al., 2021). Taking these endmember values into Equation (1), we obtain:

$$\Delta^{199}\mathrm{Hg}_{\mathrm{sample}} = 0.4 - 0.54 \times f_t - 0.4 \times f_v \quad (2)$$

Thus, the terrestrial sources fraction (f_t) can be calculated by

$$f_t = (0.4 - 0.4 \times f_v - \Delta^{199}\mathrm{Hg}_{\mathrm{sample}})/0.54 \quad (3)$$

When $f_v = 0$, representing no volcanogenic Hg input, the maximum fraction of terrestrial inputs ($f_{t\text{-max}}$) will be: $f_{t-max} =$

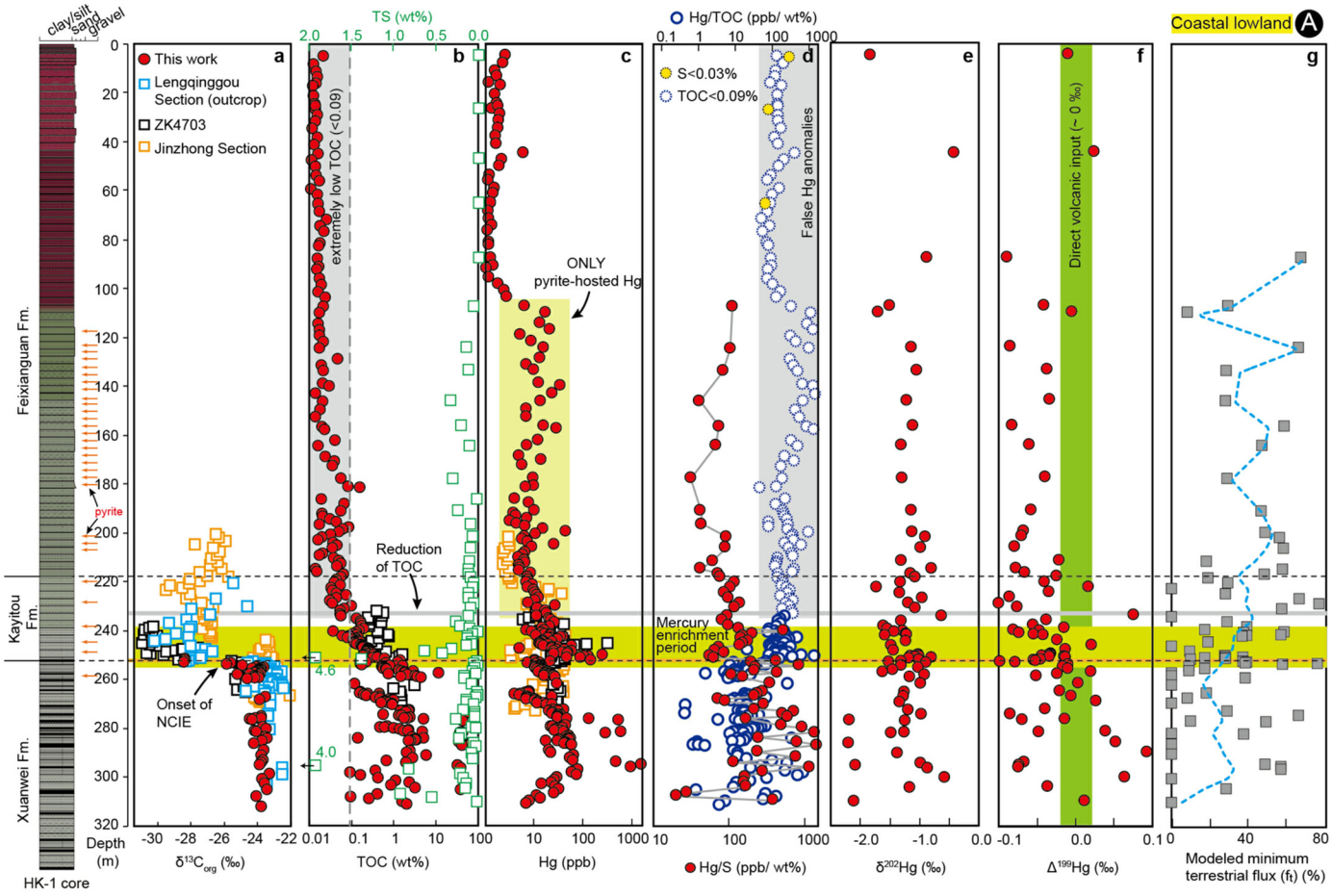

Fig. 2. Composite plots of $\delta^{13}C_{org}$, TOC, TS, Hg concentrations, Hg-anomalies (Hg/TOC, Hg/S or Hg/Al depending on the correlation between Hg and its potential hosts), Hg isotopes (δ^{202}Hg and Δ^{199}Hg), and modeled $f_{t\text{-}min}$ results for the drill core HK-1 (**A**) and TK-1 (**B**). In Figure A (upper), data of the Lengqingou Section are from Cai et al. (2021), ZK4703 from Chu et al. (2020), and Jinzhong Section from Wang et al. (2021). In Figure B, data of the Lubei Section are from Zhang et al. (2021), Guanbachong Section from Zhang et al. (2016), and the Chahe Section from Wang et al. (2021). For panel **b**: notice the reverse x-coordinate for TS content to avoid overlapping TS and TOC; the gray zone shows extremely low TOC contents (< 0.09 wt%, equal to three times the determination limit). **c**: yellow zone represents Hg sequestration by sulfides. **d**: gray zone highlights the unreliable Hg anomalies defined by Hg/TOC due to the extremely low TOC contents. The yellow dots for the Hg/S profile also show questionable Hg-anomalies due to the low TS. **f**: the green rectangle indicates direct volcanic input or local volcanic emission that has not undergone long-range transport with the Δ^{199}Hg values of ~ 0‰. Uncertainties on Hg isotope data correspond to the larger value of either the measurement uncertainty of replicate digests of GSS-5 or the uncertainty of repeated measurements of NIST 8610 (UM-Almadén). For the Δ^{199}Hg data of our samples, we used the identical value of ± 0.05‰ from GSS-5, and therefore error bars of each measured Δ^{199}Hg datapoints were not shown. **g**: the blue dashed line is the LOWESS (locally weighted scatterplot smoothing) curve through the modeled minimum terrestrial flux, which shows in percentage. NICE: negative carbon isotope excursion.

$(0.4 - \Delta^{199}Hg_{sample})/0.54$. Due to the linear relationship between $f_{t\text{-}max}$ and Δ^{199}Hg, the curve of $f_{t\text{-}max}$ would mimic that of Δ^{199}Hg and therefore was not plotted in Fig. 2.

When f_v increases from 0 to 1, representing gradually increasing portions of volcanogenic input and correspondingly decreasing contributions from terrestrial and/or atmospheric deposition, it will yield the minimum fraction of terrestrial inputs ($f_{t\text{-}min}$) in each measured sample (Fig. 2), which is valid when calculated $f_t < (1 - f_v)$. For detailed results of this model, please refer to the supplementary dataset.

3. Results

3.1. Bulk organic carbon isotopes

In the HK-1 core (Lengqinggou section, see Fig. S1), the average value of bulk $\delta^{13}C_{org}$ from 314.33 m to 252.66 m is −24.0‰, and this value decreases dramatically to −28.3‰ for the overlying strata from 252.24 m to 250.73 m (Fig. 2). This abrupt $\delta^{13}C_{org}$ negative excursion of ~4‰ has been recognized from outcrops in the same section (Cai et al., 2021). In the terrestrial TK-1 core (Taoshujing section, see Fig. S1), bulk $\delta^{13}C_{org}$ of the Xuanwei Fm. (from 178.63 m to 115.50 m) average around −22.6‰ ranging from −23.4 to −21.9‰; whereas the $\delta^{13}C_{org}$ of the overlying Kayitou Fm. from 109.70 m to 77.45 m displays a mean value of −23.4‰ ranging from −24.6 to −22.5‰. This negative shift of the bulk $\delta^{13}C_{org}$ values has also been documented in outcrops of the Taoshujing Section and other adjacent sections, consistent with the negative $\delta^{13}C_{org}$ excursion in coastal sections (Shen et al., 2011; Zhang et al., 2016).

3.2. Hg concentrations and its isotopes

While the Hg contents show an apparent decreasing trend upward in both cores, the two coeval cores displayed completely different Hg enrichment signatures. HK-1 core was formed in the coastal area and had much higher Hg contents. The Hg contents in the upper Permian Xuanwei Fm. range from 4.2 to 1571.8 ppb with a mean of ~68.2 ppb. There was a dramatic decrease upwards, with peak values occurring at the bottom of the Permian-Triassic transitional Kayitou Fm., ranging from 5.3 to 257.3 ppb (mean of ~31.5 ppb). The lowest Hg contents were observed in the Lower Triassic Feixianguan Fm., with a range from 1.1 to 45.5 ppb (mean of ~7.3 ppb). In contrast, the TK-1 core was formed in alluvial

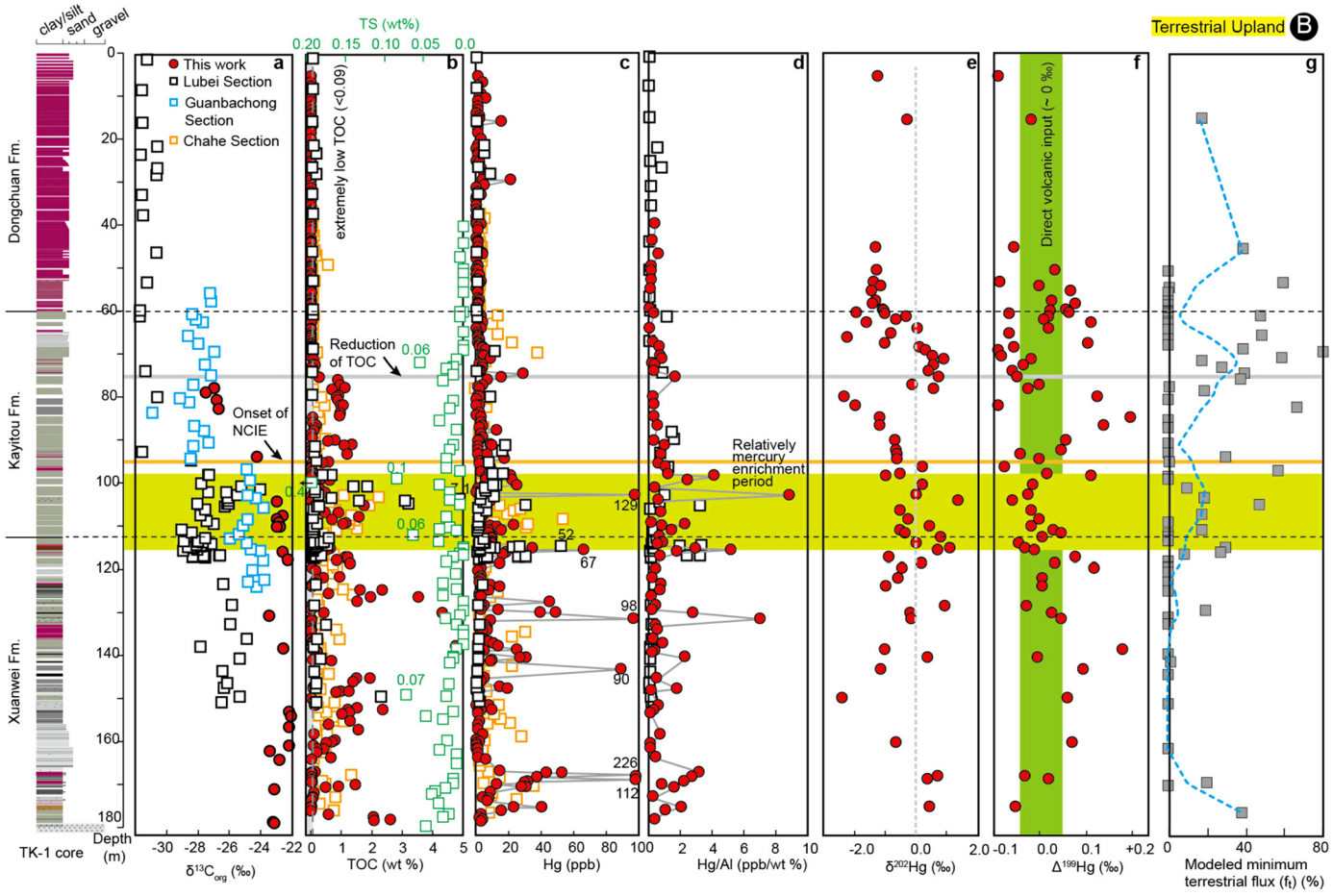

Fig. 2. (*continued*)

environments possessing purely terrestrial deposits and showing significantly lower Hg concentrations, with 0.9–226.2 ppb (mean of 15.8 ppb), 0.7–129.1 ppb (mean of 7.3 ppb), 0.6–21.7 ppb (mean of 2.5 ppb) for the Xuanwei, Kayitou, and Dongchuan formations, respectively.

δ^{202}Hg in the HK-1 core exhibits consistently negative values ranging from −2.2‰ to −0.1‰ with a mean of −1.23‰, while the TK-1 core shows more positive compositions with a range of −2.7‰ to 1.4‰ with a mean of −0.46‰. Δ^{199}Hg values in the HK-1 core vary from −0.10 to +0.09‰ with a mean of −0.04‰, with most values < 0‰. Samples with Hg concentrations >90 ppb typically exhibit much more negative Δ^{199}Hg values (Fig. 3). In the TK-1 core, Δ^{199}Hg values fluctuate around 0‰, ranging from −0.26 to +0.30‰ with an average of +0.01‰ (Figs. 2, 3).

4. Discussion

4.1. Diverse mercury host phases in non-marine sediments

Sedimentary mercury enrichment is strongly controlled by its sequestration matrix, even though an increased atmospheric Hg flux due to intensive volcanism can theoretically lead to enhanced mercury loading in marine and terrestrial sediments (Grasby et al., 2019). Under normal conditions, the contents of Hg correlate well with TOC since organic matter (OM) commonly represents the dominant phase of Hg, particularly in marine sediments (Grasby et al., 2019); sulfides and clay minerals may override the usual sedimentary Hg–TOC relationship in certain conditions (Sanei et al., 2012; Percival et al., 2018). In this work, however, we found that: (1) mercury in these non-marine sediments is associated with many different host phases, rather than a single host. (2) Alternatively, Hg mainly exists as dispersed phases without any main host minerals or materials for the OM-rich Xuanwei Fm. of the coastal HK-1 core. None of the common hosts can account for its Hg enrichment, given the moderate to weak correlation between Hg and TS ($r = +0.53$; $p < 0.0008$), Al ($r = -0.55$; $p < 0.0005$) or TOC ($r = +0.36$; $p < 0.0001$) (Fig. 4).

Previous research suggested that sulfides can effectively remove Hg from an aqueous solution within a wide pH range when organic matter burial is limited (Ehrhardt et al., 2000; Behra et al., 2001). In the OM-poor sediments from the Kayitou and Feixianguan formations of the same drill core HK-1, pyrites are the host matrix of mercury based on the strong correlation between Hg and S (Fig. 4). Moreover, Hg exhibits a relatively good correlation with TOC ($r = +0.48$; $p < 0.0001$) and Al ($r = +0.56$; $p < 0.0056$) for samples in the Kayitou Fm., indicating more influence by terrestrial sources compared with the Feixianguan Fm., where Hg only shows a strong correlation with sulfur. For the OM-limited TK-1 core from terrestrial upland, clays are more critical for Hg sequestration than OM and sulfides (Fig. 4), consistent with previous studies in the same area (Shen et al., 2019a; Chu et al., 2020; Wang et al., 2021).

4.2. Discrepant Hg signatures across different geographic settings

One of the most interesting findings in our work is the incongruent sedimentary Hg signatures between terrestrial upland and coastal lowland records. Major terrestrial Hg reservoirs are formed by accumulation of vegetation that mostly assimilates atmospheric Hg(0) of odd-MIF and subsequent burial in soils (Them et al., 2019; Zhou et al., 2021), which may get released due to

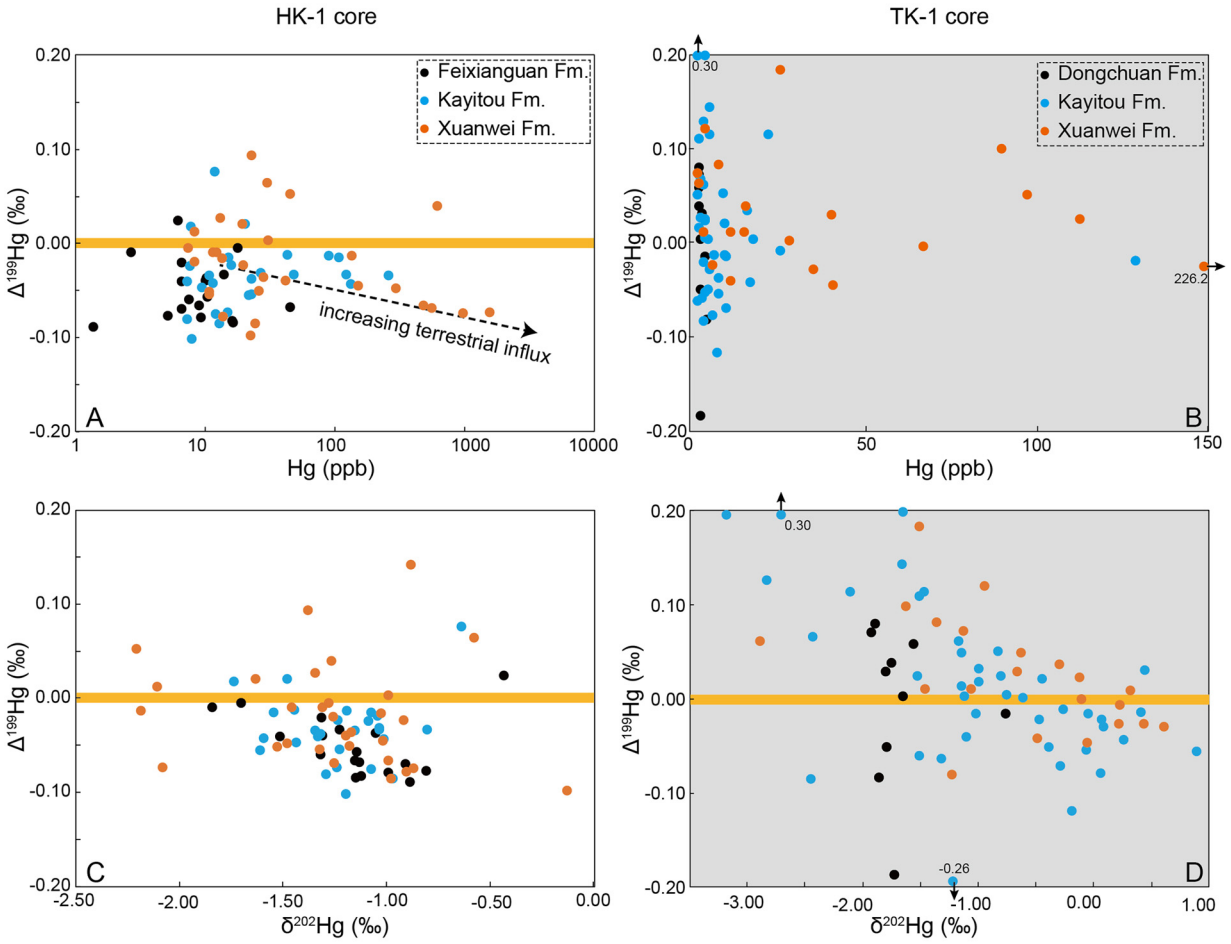

Fig. 3. Cross-plots of Δ^{199}Hg versus Hg concentration and δ^{202}Hg from the HK-1 core (**A**, **C**) and the TK-1 core (**B**, **D**).

terrestrial environment change, dominating the Hg enrichment in nearshore sediments. Thus, intensified wildfires and the combustion of sedimentary hydrocarbons during the EPME have been proposed as the leading cause of the mercury spike in shallow marine sections (Kaiho et al., 2021). Investigation of modern sediments suggests that riverine input represents the largest source of Hg in the coastal area due to terrestrial effects (e.g., increased input of eroded soil or plant material) (Liu et al., 2021). Given that shallow-marine has been significantly influenced by terrestrial Hg influx (Grasby et al., 2017; Wang et al., 2018), non-marine sediments should have more terrestrial sources resulting from the environmental disruption on land (Grasby et al., 2017; Them et al., 2019).

In the HK-1 core, peak values of Hg anomalies defined by Hg/TOC occurred from the Xuanwei Fm. to the basal Kayitou Fm. (Fig. 2A), slightly later than the onset of the negative carbon isotope excursion (NCIE) and nadirs of $\delta^{13}C_{org}$ values. These decoupled C and Hg records were previously interpreted as evidence of multiple possible sources for both elements, such as volcanic, thermogenic or wildfire release (Chu et al., 2020). Although our new evidence of the consistently negative δ^{202}Hg values ($\sim -2‰$ to 0‰) preserved in the ancient coastal sediments cannot distinguish the Hg sources, their mostly negative Δ^{199}Hg signatures strongly suggest predominant terrestrial input (Figs. 2, 3). According to our model, the averaged minimum terrestrial influx into coastal sediments has increased upward the profile (Fig. 2), with several peak values of the modeled $f_{t\text{-}min}$ occurring within the mercury enrichment horizon, indicating the mercury anomalies were mainly caused by terrestrial sources. Above the mercury-rich interval, the lower Hg concentration occurs in the OM-poor sediments (TOC < 0.09 wt%, i.e., less than three times the determination limit), which can be caused by oxidation or post-depositional weathering (Charbonnier et al., 2020; Liu et al., 2022; Park et al., 2022). Particularly, the purple-red sequences above the depth of 107.40 m likely result from oxidation under warm and dry conditions during the earliest Triassic (Zhang et al., 2016). Hg anomalies constrained by Hg/S ratios decline also indicate a decreased Hg input with negative Δ^{199}Hg values, especially for the pyrite-hosted mercury, likely suggesting continuous but lesser terrestrial influx (Fig. 2). An alternative interpretation is the redox control as the negative Δ^{199}Hg value could be generated under euxinia (Zheng et al., 2018), which will be discussed further in Section 4.3 followed.

Unlike coastal sediments, most of the TK-1 core from terrestrial upland displays much lower Hg contents showing stronger covariation with the content of Al (Fig. 4), and thus Hg/Al ratios are used for Hg normalization and referred to as Hg anomalies (Fig. 2B). The relative mercury-anomaly period at a depth of 98.54 to 115.80 m has both δ^{202}Hg and Δ^{199}Hg values fluctuating around 0‰, consistent with previous work on the same depositional environment, which was interpreted as influenced by the STLIP (Shen et al., 2019b), or felsic volcanic eruptions related to the subduction (Shen et al., 2021; Zhang et al., 2021). A small pulse of Hg enrichment with distinct negative Δ^{199}Hg values occurs immediately after the reduction of TOC at a depth of ~60 to 75 m, which likely suggests a lesser extent of terrestrial influx and could be verified by our model, showing peaks of minimum terrestrial flux (Fig. 2). However, given the average Hg compositions of the upper continental crust and sedimentary rocks are 50 ppb (Rudnick and Gao, 2014) and 62.4 ppb (Grasby et al., 2019), respectively, it seems more

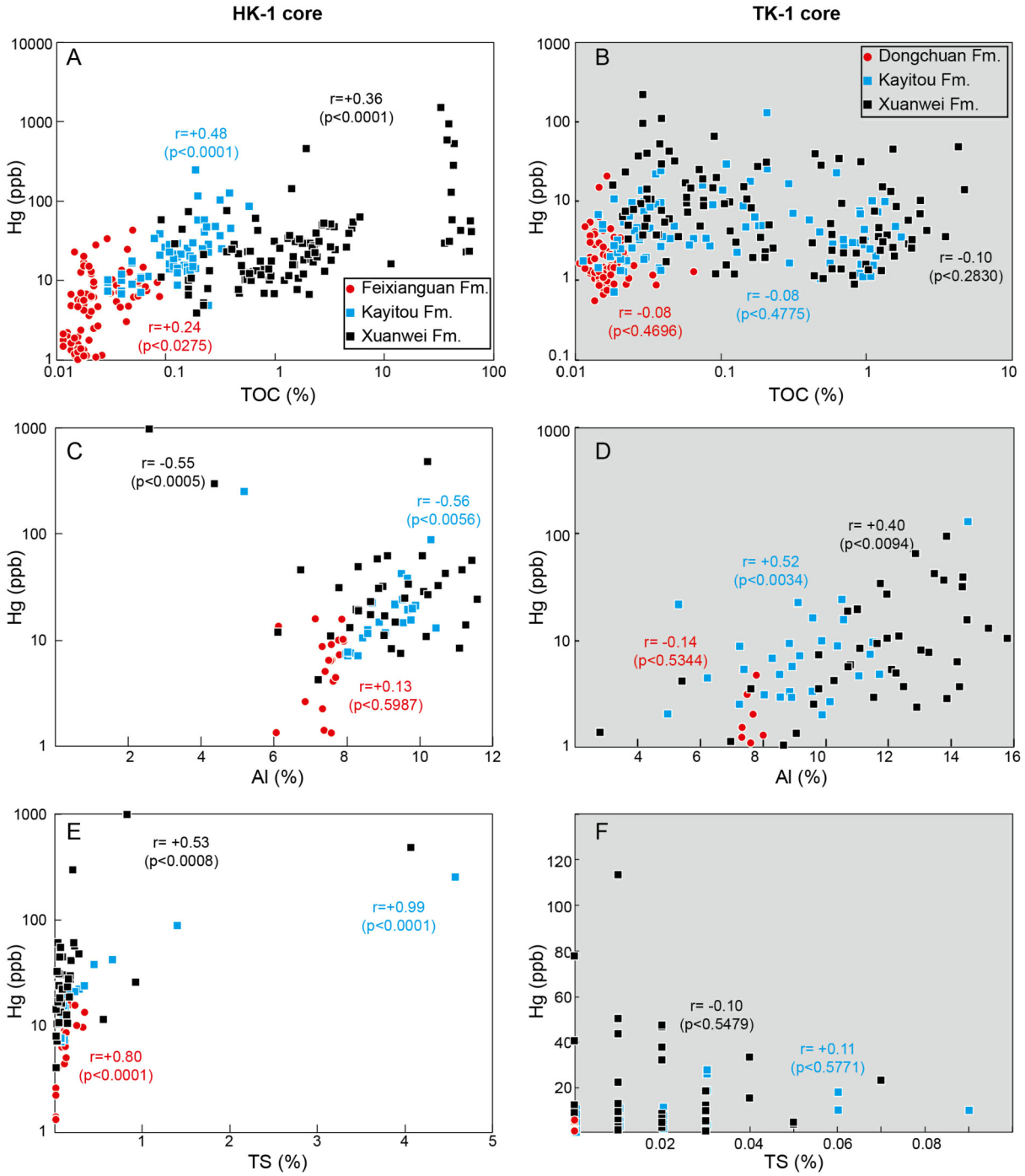

Fig. 4. Correlations between elemental Hg and its potential host matrix — organic matter, clay minerals, and sulfide. Data for all the left panels (A, C, E) are from the HK-1 core, and right panels (B, D, F) are from the TK-1 core.

reasonable that our measured sediments did not have Hg enrichment, but only reflected background Hg signatures. The fluctuating Δ^{199}Hg values between slightly negative to slightly positive could result from the changes in the proportions of terrestrial and atmospheric depositions, rather than volcanic input, consistent with the low values of our modeled minimum terrestrial flux ($f_{t\text{-}min}$).

Both drill cores exhibit relatively high Hg concentrations and Hg anomalies characterized by Hg/S, Hg/TOC or Hg/Al ratios from the upper Xuanwei Fm. to the basal Kayitou Fm. Moreover, the underlying Xuanwei Fm. displays occasional Hg spikes with positive Hg-MIF values (Fig. 2). At present, no changes of the terrestrial environment, such as enhanced continental erosion, increased runoff, or terrestrial influx, have been reported during the depositional time of this formation. However, despite the stable sedimentary environment, the Xuanwei Fm. has exhibited spikes in both Hg-MIF values and Hg enrichment. This could be the result of additional sources, such as pulsed deposition due to volcanic outgassing that has undergone long-range transport. The exact timing and origin of these pulsed volcanic sources are difficult to determine based on the existing evidence in the current study and other previous studies. Nevertheless, the active volcanic arcs that surrounded the margin of the supercontinent Pangea at the end of Permian (Chapman et al., 2022) or even in the early eruption of STLIP (Burgess et al., 2017) could be the possible reason.

4.3. Local environment factors controlling sedimentary Hg

Noticeably, the mercury enrichment horizon in both drill cores does not correspond to the NCIE in this work. Given the extremely high-resolution sampling strategy and their stable sedimentary environments, this decoupling of Hg and C indicates that these two elements are controlled by different sources, as discussed above, or alternatively, local environmental factors in both different non-marine settings. As the HK-1 and TK-1 drill cores are only ~70 km away from each other (Fig. S1), the discrepant Hg signatures between the two cores most likely result from local factors. In the HK-1 core, moderate positive correlation between the content of Hg and total sulfur in the Xuanwei Fm. changed to a strong positive correlation in the overlying strata (Fig. 4). The coastal area has substantial supplies of terrestrial-derived OM and sulfate, where the dynamic equilibrium between the intensive generation of reduced sulfur makes it possible for the development of photic zone euxinia (PZE) in the anoxic water column and underlying sediments. A recent study indicates that sediments deposited under the PZE tend to develop significantly more negative Δ^{199}Hg values than those deposited under non-PZE conditions (Zheng et al., 2018). The negative Δ^{199}Hg was considered to be caused by photoreduction of Hg (II) complexed by reduced sulfur ligands in a sulfide-rich environment or enhanced sequestration of atmospheric Hg (0) to sediments. The coastal HK-1 core has relatively high sulfur contents and substantial pyrite layers (Fig. 2A), so anoxic and sulfidic water development could account for the negative Δ^{199}Hg values, which was also supported by the lack of correlation between Hg and Al, as well as the strongest correlation between Hg and TS in the Feixianguan Fm. (Fig. 4). Moreover, local euxinic conditions have developed in the coastal lowland, documented by the positive relationship between Hg and chalcophile elements, like Mo, Se, and Co (Fig. 5).

4.4. Broader implications: possibly asynchronous terrestrial ecosystem disturbance

The relatively high TOC interval occurring at ~74–84 m in the TK-1 core above the most negative $\delta^{13}C_{org}$ value in this study has been previously documented in a nearby drill core ZK4703 by Chu et al. (2020), but the amplitude in the latter core is much smaller than our core. By contrast, a high TOC value has not been recognized in other terrestrial or coastal sediments in the studied area (Shen et al., 2019b; Chu et al., 2020; Wang et al., 2021). Therefore, a high TOC content is probably controlled by the local depositional environment and should not be used as a tool for stratigraphic correlation. Previous studies demonstrated that carbon isotopes from marine PTB sections display distinctive negative excursions in both inorganic and organic $\delta^{13}C$, and therefore the most negative $\delta^{13}C_{org}$ values have been widely used to correlate marine sequences and constrain the PTB in non-marine sequences worldwide (de Wit et al., 2002; Cao et al., 2008; Hermann et al., 2010; Shen et al., 2011; Zhang et al., 2016). If the period from the onset of the negative $\delta^{13}C_{org}$ excursion to its minimum (OTM zone in Fig. 6) were synchronous in all depositional environments, including marine and non-marine, our results might indicate a diachronic terrestrial disturbance associated with discrepant mercury deposition across facies from the terrestrial upland to the coastal lowland and the shallow marine in South China (Fig. 6).

The previous reports on fossil records have documented a diachronic pattern of vegetation turnover in different environments across the Permian–Triassic transition in the study area (Feng et al., 2020a, 2020b). In the upland environments, the species richness of the Cathaysian Flora declined dramatically at the bottom of the Kayitou Fm. compared with the underlying Xuanwei Fm. (Feng et al., 2020a, 2020b; Liu et al., 2020). While in the coastal lowland environments, the specific diversity of the Cathaysia Flora likely persisted continuously into the lowermost part of the Kayitou Fm. At ~2 meters above the Kayitou–Xuanwei formation boundary in the coastal sections, the Cathaysian Flora disappeared eventually and was replaced by monospecific vegetations comprising herbaceous lycophytes, *Tomiostrobus sinensis* Feng 2020 (Feng et al., 2020b). As discussed above, the coastal lowland HK-1 core exhibits Hg enrichments by predominant terrestrial sources occurring from the upper Xuanwei Fm. to the basal Kayitou Fm., while the upland core TK-1 shows weaker Hg enrichments with limited terrestrial and/or atmospheric inputs in the same horizon. Recent geochronological studies on the high-precision zircon U-Pb of the ash beds in the study area have documented that the Kayitou Fm. in the

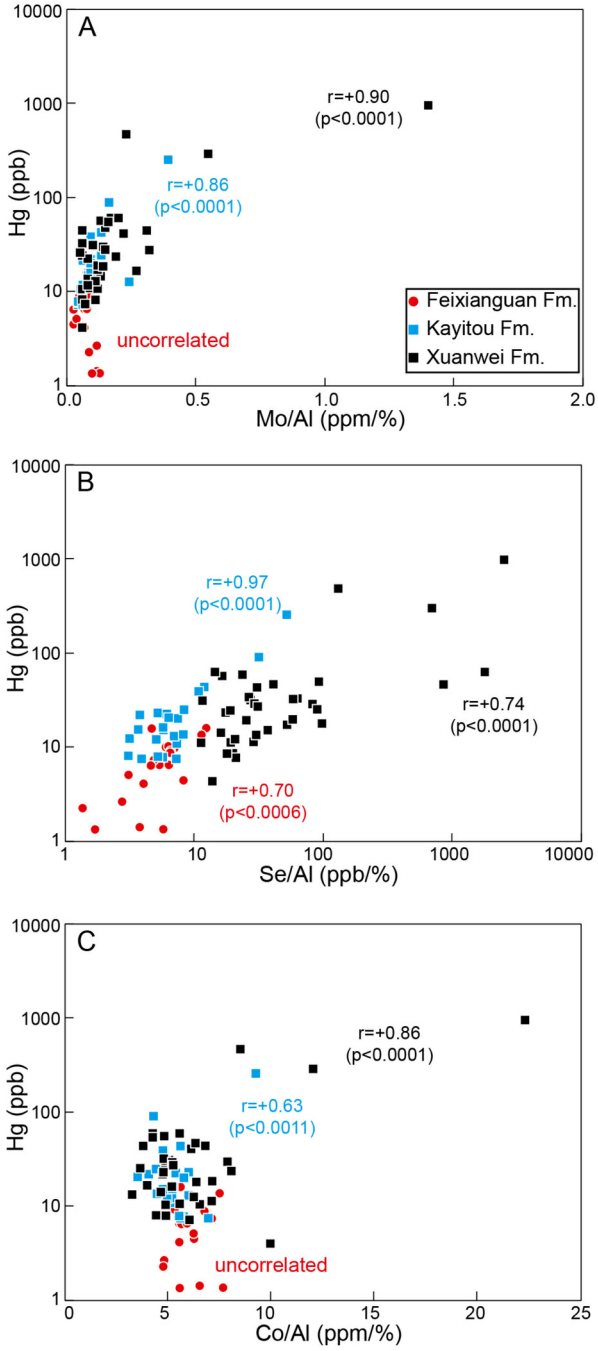

Fig. 5. Correlations between the Hg content and redox-sensitive chalcophile elements (Mo, Se, and Co) in the HK-1 core.

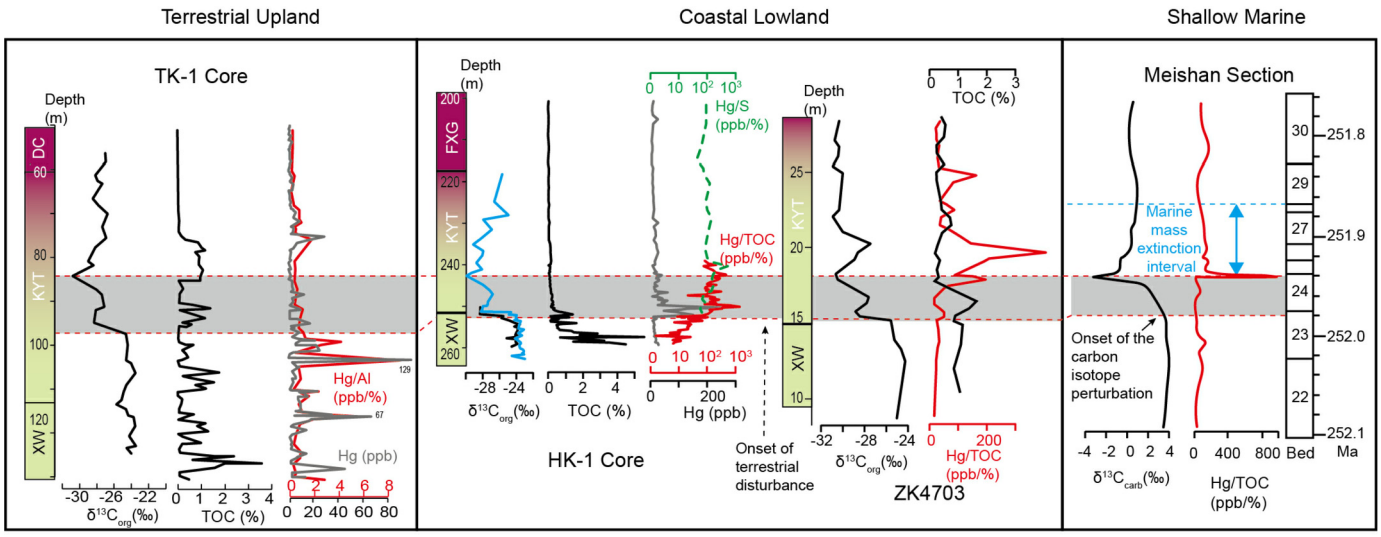

Fig. 6. Lateral comparison of $\delta^{13}C$, TOC, Hg contents or Hg-anomalies across different PTB sedimentary facies from terrestrial upland and coastal lowland to shallow marine in South China. The gray zone represents an interval of carbon perturbation defined from the onset of negative carbon isotope excursion to the most negative values (OTM) that are emphasized by two red dashed lines. Notice that Hg anomalies of various facies matched differently with the OTM. Other data sources: Blue line are $\delta^{13}C$ data from outcrops at the same location of core HK-1 (Cai et al., 2021); profiles of $\delta^{13}C$, TOC, and Hg/TOC in ZK4703 modified from (Chu et al., 2020); data for Meishan section from (Grasby et al., 2017).

coastal settings (Early Triassic) is much younger in age than that in the upland settings (latest Permian) (Wu, 2020), and therefore indicate that the collapse of the Cathaysian Flora initially occurred in the upland environments but later in the coastal region. Our discrepant mercury records in different geological settings (Fig. 6), likely reinforced the diachronic scenario of the terrestrial ecosystem collapse associated with intensive wildfires (Cai et al., 2021).

5. Conclusions

Sedimentary Hg enrichments around the PTB have been widely regarded as direct evidence supporting a causal link between volcanism and the EPME in both marine and terrestrial environments. Our work from two different non-marine drill cores shows discrepant mercury records of terrestrial upland versus coastal lowland, which compromise the Hg anomalies as indicators of volcanism. In addition, Hg signals from these two settings are most likely explained by asynchronous vegetational collapses and consequent weathering across the upland to the lowland straddling the PTB. Composite factors like Hg concentration, Hg isotope, and local environmental indicators should be considered before any Hg enrichments are directly linked with possible volcanic activities.

CRediT authorship contribution statement

S.Z.S. and Z.F. conceived and led the study. J.C. conducted core logging & sampling; J.C. and G.Y.S. designed the experiments; J.C., G.Y.S., B.J.L., R.Y.M., and Z.X. performed experiments; J.C., G.Y.S., H.Z., S.Z.S., F.F.Z., and Z.F. analyzed the data; J.C., F.F.Z., and Z.F. wrote the paper with input from coauthors. All authors read and approved the submitted version of the manuscript.

Declaration of competing interest

The authors declare that they have no known competing financial interests or personal relationships that could have appeared to influence the work reported in this paper.

Data availability

The geochemical data generated in this study are provided in Supplementary Data S2 to S3. The detailed procedures for our ternary mixing model are provided in Supplementary Data S4. More data will be made available on request.

Acknowledgements

We thank Hai-Bo Wei, Hang-Yu Liu, Xu-Dong Gou, Xin-Shi Cheng, and Fu-Guang Zhao for their fieldwork assistance. Thanks also to Jun Shen and Xiangdong Wang from the China University of Geosciences (Wuhan) for providing their published dataset. This study was financially supported by the State Key Laboratory of Palaeobiology and Stratigraphy (Nanjing Institute of Geology and Palaeontology, CAS) (223105), Strategic Priority Research Program of the Chinese Academy of Sciences (XDB26000000), Second Tibetan Plateau Scientific Expedition and Research (2019QZKK0706), the Key Research Program of the Institute of Geology and Geophysics, Chinese Academy of Sciences (IGGCAS-201905) and National Natural Science Foundation of China (42293280, 42261144668, 42073002). F.F.Z. acknowledges financial support from the Fundamental Research Funds for the Central Universities (0206-14912213, 0206/14380149) and Frontiers Science Center for Critical Earth Material Cycling Fund (DLTD2102). We thank Andrew Jacobson and two anonymous reviewers for their insightful suggestions that have greatly improved our work.

Appendix A. Supplementary material

Supplementary material related to this article can be found online at https://doi.org/10.1016/j.epsl.2023.118195.

References

Behra, P., Bonnissel-Gissinger, P., Alnot, M., Revel, R., Ehrhardt, J.J., 2001. XPS and XAS study of the sorption of Hg(II) onto pyrite. Langmuir 17, 3970–3979. https://doi.org/10.1021/la0014510.

Bergquist, B.A., 2017. Mercury, volcanism, and mass extinctions. Proc. Natl. Acad. Sci. USA 114, 8675–8677. https://doi.org/10.1073/pnas.1709070114.

Biswas, A., Blum, J.D., Bergquist, B.A., Keeler, G.J., Xie, Z., 2008. Natural mercury isotope variation in coal deposits and organic soils. Environ. Sci. Technol. 42, 8303–8309. https://doi.org/10.1021/es801444b.

Blum, J.D., Johnson, M.W., 2017. Recent developments in mercury stable isotope analysis. Rev. Mineral. Geochem. 82, 733–757. https://doi.org/10.2138/rmg.2017.82.17.

Blum, J.D., Sherman, L.S., Johnson, M.W., 2014. Mercury isotopes in Earth and environmental sciences. Annu. Rev. Earth Planet. Sci. 42, 249–269. https://doi.org/10.1146/annurev-earth-050212-124107.

Burgess, S.D., Muirhead, J.D., Bowring, S.A., 2017. Initial pulse of Siberian Traps sills as the trigger of the end-Permian mass extinction. Nat. Commun. 8, 164. https://doi.org/10.1038/s41467-017-00083-9.

Cai, Y., Zhang, H., Feng, Z., Shen, S., 2021. Intensive wildfire associated with volcanism promoted the vegetation changeover in Southwest China during the Permian–Triassic transition. Front. Earth Sci. 9, 615841. https://doi.org/10.3389/feart.2021.615841.

Cao, C., Wang, W., Liu, L., Shen, S., Summons, R.E., 2008. Two episodes of ^{13}C-depletion in organic carbon in the latest Permian: evidence from the terrestrial sequences in northern Xinjiang, China. Earth Planet. Sci. Lett. 270, 251–257. https://doi.org/10.1016/j.epsl.2008.03.043.

Chapman, T., Milan, L.A., Metcalfe, I., Blevin, P.L., Crowley, J., 2022. Pulses in silicic arc magmatism initiate end-Permian climate instability and extinction. Nat. Geosci. 15, 411–416. https://doi.org/10.1038/s41561-022-00934-1.

Charbonnier, G., Adatte, T., Föllmi, K.B., Suan, G., 2020. Effect of intense weathering and postdepositional degradation of organic matter on Hg/TOC proxy in organic-rich sediments and its implications for deep-time investigations. Geochem. Geophys. Geosyst. 21, e2019GC008707. https://doi.org/10.1029/2019GC008707.

Chen, J., Guo, Y., Wei, H.-B., Liu, H.-Y., Ma, R.-Y., Xiao, Z., Feng, Z., 2022. Evaluation of chemical weathering proxies by comparing drilled cores versus outcrops and weathering history during the Permian–Triassic transition. Glob. Planet. Change 214, 103855. https://doi.org/10.1016/j.gloplacha.2022.103855.

Chen, J., Hintelmann, H., Feng, X., Dimock, B., 2012. Unusual fractionation of both odd and even mercury isotopes in precipitation from Peterborough, ON, Canada. Geochim. Cosmochim. Acta 90, 33–46. https://doi.org/10.1016/j.gca.2012.05.005.

Chen, J., Xu, Y., 2019. Establishing the link between Permian volcanism and biodiversity changes: insights from geochemical proxies. Gondwana Res. 75, 68–96. https://doi.org/10.1016/j.gr.2019.04.008.

Chu, D., Dal Corso, J., Shu, W., Song, H., Wignall, P.B., Grasby, S.E., van de Schootbrugge, B., Zong, K., Wu, Y., Tong, J., 2021. Metal-induced stress in survivor plants following the end-Permian collapse of land ecosystems. Geology 49, 657–661. https://doi.org/10.1130/G48333.1.

Chu, D., Grasby, S.E., Song, Haijun, Dal Corso, J., Wang, Y., Mather, T.A., Wu, Y., Song, Huyue, Shu, W., Tong, J., Wignall, P.B., 2020. Ecological disturbance in tropical peatlands prior to marine Permian-Triassic mass extinction. Geology 48, 288–292. https://doi.org/10.1130/G46631.1.

de Wit, M.J., Ghosh, J.G., de Villiers, S., Rakotosolofo, N., Alexander, J., Tripathi, A., Looy, C., 2002. Multiple organic carbon isotope reversals across the Permo-Triassic boundary of terrestrial Gondwana sequences: clues to extinction patterns and delayed ecosystem recovery. J. Geol. 110, 227–240. https://doi.org/10.1086/338411.

Ehrhardt, J.-J., Behra, P., Bonnissel-Gissinger, P., Alnot, M., 2000. XPS study of the sorption of Hg(II) onto pyrite FeS_2. Surf. Interface Anal. 30, 269–272. https://doi.org/10.1002/1096-9918(200008)30:1<269::AID-SIA758>3.0.CO;2-N.

Fan, J., Shen, S., Erwin, D.H., Sadler, P.M., MacLeod, N., Cheng, Q., Hou, X., Yang, J., Wang, X., Wang, Y., Zhang, H., Chen, X., Li, G., Zhang, Y., Shi, Y., Yuan, D., Chen, Q., Zhang, L., Li, C., Zhao, Y., 2020. A high-resolution summary of Cambrian to Early Triassic marine invertebrate biodiversity. Science 367, 272–277. https://doi.org/10.1126/science.aax4953.

Feng, Z., Wei, H., Ye, R., Sui, Q., Gou, X., Guo, Y., Liu, L., Yang, S., 2020a. Latest Permian peltasperm plant from Southwest China and its paleoenvironmental implications. Front. Earth Sci. 8, 559430. https://doi.org/10.3389/feart.2020.559430.

Feng, Z., Wei, H.-B., Guo, Y., He, X.-Y., Sui, Q., Zhou, Y., Liu, H.-Y., Gou, X.-D., Lv, Y., 2020b. From rainforest to herbland: New insights into land plant responses to the end-Permian mass extinction. Earth-Sci. Rev. 204, 103153. https://doi.org/10.1016/j.earscirev.2020.103153.

Grasby, S.E., Shen, W., Yin, R., Gleason, J.D., Blum, J.D., Lepak, R.F., Hurley, J.P., Beauchamp, B., 2017. Isotopic signatures of mercury contamination in latest Permian oceans. Geology 45, 55–58. https://doi.org/10.1130/G38487.1.

Grasby, S.E., Them, T.R., Chen, Z., Yin, R., Ardakani, O.H., 2019. Mercury as a proxy for volcanic emissions in the geologic record. Earth-Sci. Rev. 196, 102880. https://doi.org/10.1016/j.earscirev.2019.102880.

Hermann, E., Hochuli, P.A., Bucher, H., Vigran, J.O., Weissert, H., Bernasconi, S.M., 2010. A close-up view of the Permian–Triassic boundary based on expanded organic carbon isotope records from Norway (Trøndelag and Finnmark Platform). Glob. Planet. Change 74, 156–167. https://doi.org/10.1016/j.gloplacha.2010.10.007.

Jiskra, M., Heimbürger-Boavida, L.-E., Desgranges, M.-M., Petrova, M.V., Dufour, A., Ferreira-Araujo, B., Masbou, J., Chmeleff, J., Thyssen, M., Point, D., Sonke, J.E., 2021. Mercury stable isotopes constrain atmospheric sources to the ocean. Nature 597, 678–682. https://doi.org/10.1038/s41586-021-03859-8.

Kaiho, K., Aftabuzzaman, Md., Jones, D.S., Tian, L., 2021. Pulsed volcanic combustion events coincident with the end-Permian terrestrial disturbance and the following global crisis. Geology 49, 289–293. https://doi.org/10.1130/G48022.1.

Liu, H.-Y., Wei, H.-B., Chen, J., Guo, Y., Zhou, Y., Gou, X.-D., Yang, S.-L., Labandeira, C., Feng, Z., 2020. A latitudinal gradient of plant–insect interactions during the late Permian in terrestrial ecosystems? New evidence from Southwest China. Glob. Planet. Change 192, 103248. https://doi.org/10.1016/j.gloplacha.2020.103248.

Liu, M., Zhang, Q., Maavara, T., Liu, S., Wang, X., Raymond, P.A., 2021. Rivers as the largest source of mercury to coastal oceans worldwide. Nat. Geosci. 14, 672–677. https://doi.org/10.1038/s41561-021-00793-2.

Liu, Z., Tian, H., Yin, R., Chen, D., Gai, H., 2022. Mercury loss and isotope fractionation during thermal maturation of organic-rich mudrocks. Chem. Geol. 612, 121144. https://doi.org/10.1016/j.chemgeo.2022.121144.

Lyman, S.N., Cheng, I., Gratz, L.E., Weiss-Penzias, P., Zhang, L., 2020. An updated review of atmospheric mercury. Sci. Total Environ. 707, 135575. https://doi.org/10.1016/j.scitotenv.2019.135575.

Park, J., Stein, H.J., Georgiev, S.V., Hannah, J.L., 2022. Degradation of Hg signals on incipient weathering: Core versus outcrop geochemistry of Upper Permian shales, East Greenland and Mid-Norwegian Shelf. Chem. Geol. 608, 121030. https://doi.org/10.1016/j.chemgeo.2022.121030.

Percival, L.M.E., Jenkyns, H.C., Mather, T.A., Dickson, A.J., Batenburg, S.J., Ruhl, M., Hesselbo, S.P., Barclay, R., Jarvis, I., Robinson, S.A., Woelders, L., 2018. Does large igneous province volcanism always perturb the mercury cycle? Comparing the records of Oceanic Anoxic Event 2 and the end-Cretaceous to other Mesozoic events. Am. J. Sci. 318, 799–860. https://doi.org/10.2475/08.2018.01.

Pyle, D.M., Mather, T.A., 2003. The importance of volcanic emissions for the global atmospheric mercury cycle. Atmos. Environ. 37, 5115–5124. https://doi.org/10.1016/j.atmosenv.2003.07.011.

Rudnick, R.L., Gao, S., 2014. Composition of the continental crust. In: Holland, H.D., Turekian, K.K. (Eds.), Treatise on Geochemistry, second edition. Elsevier, pp. 1–51.

Sanei, H., Grasby, S.E., Beauchamp, B., 2012. Latest Permian mercury anomalies. Geology 40, 63–66. https://doi.org/10.1130/G32596.1.

Sepkoski, J.J., 1984. A kinetic model of Phanerozoic taxonomic diversity. III. Post-Paleozoic families and mass extinctions. Paleobiology 10, 246–267.

Shen, J., Algeo, T.J., Feng, Q., 2022. Mercury isotope evidence for a non-volcanic origin of Hg spikes at the Ordovician-Silurian boundary, South China. Earth Planet. Sci. Lett. 594, 117705. https://doi.org/10.1016/j.epsl.2022.117705.

Shen, J., Chen, J., Algeo, T.J., Feng, Q., Yu, J., Xu, Y.-G., Xu, G., Lei, Y., Planavsky, N.J., Xie, S., 2021. Mercury fluxes record regional volcanism in the South China craton prior to the end-Permian mass extinction. Geology 49, 452–456. https://doi.org/10.1130/G48501.1.

Shen, J., Chen, J., Algeo, T.J., Yuan, S., Feng, Q., Yu, J., Zhou, L., O'Connell, B., Planavsky, N.J., 2019a. Evidence for a prolonged Permian–Triassic extinction interval from global marine mercury records. Nat. Commun. 10, 1563. https://doi.org/10.1038/s41467-019-09620-0.

Shen, J., Yu, J., Chen, J., Algeo, T.J., Xu, G., Feng, Q., Shi, X., Planavsky, N.J., Shu, W., Xie, S., 2019b. Mercury evidence of intense volcanic effects on land during the Permian-Triassic transition. Geology 47, 1117–1121. https://doi.org/10.1130/G46679.1.

Shen, S., Crowley, J.L., Wang, Y., Bowring, S.A., Erwin, D.H., Sadler, P.M., Cao, C., Rothman, D.H., Henderson, C.M., Ramezani, J., Zhang, H., Shen, Y., Wang, X., Wang, W., Mu, L., Li, W., Tang, Y., Liu, X., Liu, L., Zeng, Y., Jiang, Y., Jin, Y., 2011. Calibrating the end-Permian mass extinction. Science 334, 1367–1372. https://doi.org/10.1126/science.1213454.

Shi, M., Bergquist, B.A., Zhou, A., Zhao, Y., Sun, R., Chen, J., Zheng, W., 2023. The efficiency of Hg cold vapor generation and its influence on Hg isotope analysis by MC-ICP-MS. J. Anal. At. Spectrom. https://doi.org/10.1039/d3ja00056g.

Si, M., McLagan, D.S., Mazot, A., Szponar, N., Bergquist, B., Lei, Y.D., Mitchell, C.P.J., Wania, F., 2020. Measurement of atmospheric mercury over volcanic and fumarolic regions on the North Island of New Zealand using passive air samplers. ACS Earth Space Chem. 4, 2435–2443. https://doi.org/10.1021/acsearthspacechem.0c00274.

Sun, R., Enrico, M., Heimbürger, L.-E., Scott, C., Sonke, J.E., 2013. A double-stage tube furnace—acid-trapping protocol for the pre-concentration of mercury from solid samples for isotopic analysis. Anal. Bioanal. Chem. 405, 6771–6781. https://doi.org/10.1007/s00216-013-7152-2.

Sun, R., Streets, D.G., Horowitz, H.M., Amos, H.M., Liu, G., Perrot, V., Toutain, J.-P., Hintelmann, H., Sunderland, E.M., Sonke, J.E., 2016. Historical (1850–2010) mercury stable isotope inventory from anthropogenic sources to the atmosphere. Elem. Sci. Anthrop. 4, 000091. https://doi.org/10.12952/journal.elementa.000091.

Them, T.R., Jagoe, C.H., Caruthers, A.H., Gill, B.C., Grasby, S.E., Gröcke, D.R., Yin, R., Owens, J.D., 2019. Terrestrial sources as the primary delivery mechanism of mercury to the oceans across the Toarcian Oceanic Anoxic Event (Early Jurassic). Earth Planet. Sci. Lett. 507, 62–72. https://doi.org/10.1016/j.epsl.2018.11.029.

Wang, X., Cawood, P.A., Grasby, S.E., Zhao, L., Chen, Z.-Q., Wu, S., Yuangeng, H., 2021. Characteristics of Hg concentrations and isotopes in terrestrial and marine facies across the end-Permian mass extinction. Glob. Planet. Change 205, 103592. https://doi.org/10.1016/j.gloplacha.2021.103592.

Wang, X., Cawood, P.A., Zhao, H., Zhao, L., Grasby, S.E., Chen, Z.-Q., Wignall, P.B., Lv, Z., Han, C., 2018. Mercury anomalies across the end-Permian mass extinction in South China from shallow and deep water depositional environments. Earth Planet. Sci. Lett. 496, 159–167. https://doi.org/10.1016/j.epsl.2018.05.044.

Wu, Q., 2020. High-precision zircon U-Pb geochronological studies of the Permian ash beds from China and North America. Ph.D. thesis. University of Science and Technology of China (in Chinese with English abstract).

Yin, R., Feng, X., Hurley, J.P., Krabbenhoft, D.P., Lepak, R.F., Hu, R., Zhang, Q., Li, Z., Bi, X., 2016. Mercury isotopes as proxies to identify sources and environmental

impacts of mercury in sphalerites. Sci. Rep. 6, 18686. https://doi.org/10.1038/srep18686.
Zambardi, T., Sonke, J.E., Toutain, J.P., Sortino, F., Shinohara, H., 2009. Mercury emissions and stable isotopic compositions at Vulcano Island (Italy). Earth Planet. Sci. Lett. 277, 236–243. https://doi.org/10.1016/j.epsl.2008.10.023.
Zhang, H., Cao, C., Liu, X., Mu, L., Zheng, Q., Liu, F., Xiang, L., Liu, L., Shen, S., 2016. The terrestrial end-Permian mass extinction in South China. Palaeogeogr. Palaeoclimatol. Palaeoecol. 448, 108–124. https://doi.org/10.1016/j.palaeo.2015.07.002.
Zhang, H., Zhang, F., Chen, J., Erwin, D.H., Syverson, D.D., Ni, P., Rampino, M., Chi, Z., Cai, Y., Xiang, L., Li, W., Liu, S.-A., Wang, R., Wang, X., Feng, Z., Li, H., Zhang, T., Cai, H., Zheng, W., Cui, Y., Zhu, X., Hou, Z., Wu, F., Xu, Y., Planavsky, N., Shen, S., 2021. Felsic volcanism as a factor driving the end-Permian mass extinction. Sci. Adv. 7, eabh1390. https://doi.org/10.1126/sciadv.abh1390.
Zheng, W., Gilleaudeau, G.J., Kah, L.C., Anbar, A.D., 2018. Mercury isotope signatures record photic zone euxinia in the Mesoproterozoic ocean. Proc. Natl. Acad. Sci. USA 115, 10594–10599. https://doi.org/10.1073/pnas.1721733115.
Zheng, X., Dai, S., Nechaev, V., Sun, R., 2020. Environmental perturbations during the latest Permian: Evidence from organic carbon and mercury isotopes of a coal-bearing section in Yunnan Province, southwestern China. Chem. Geol. 549, 119680. https://doi.org/10.1016/j.chemgeo.2020.119680.
Zhou, J., Obrist, D., Dastoor, A., Jiskra, M., Ryjkov, A., 2021. Vegetation uptake of mercury and impacts on global cycling. Nat. Rev. Earth Environ. 2, 269–284. https://doi.org/10.1038/s43017-021-00146-y.